# Vertical growth of superconducting crystalline hollow nanowires by $He^+$ focused ion beam induced deposition

*Rosa Córdoba[1,2], Alfonso Ibarra[3], Dominique Mailly[4], and José Mª De Teresa[1,2,3]*

[1] *Instituto de Ciencia de Materiales de Aragón (ICMA), CSIC - Universidad de Zaragoza, Spain*

[2] *Departamento de Física de la Materia Condensada, Universidad de Zaragoza, 50009 Zaragoza, Spain*

[3] *Laboratorio de Microscopías Avanzadas (LMA), Instituto de Nanociencia de Aragón (INA), Universidad de Zaragoza, Spain*

[4] *Centre de Nanosciences et de Nanotechnologies, CNRS, Univ Paris Sud, Université Paris Saclay, 91120 Palaiseau, France*

Table of contents graphic

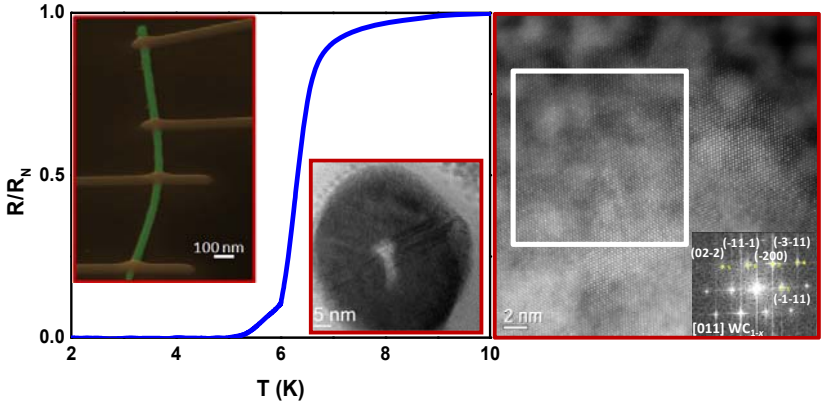


ABSTRACT 150–250 words

Novel physical properties appear when the size of a superconductor is reduced to the nanoscale, in the range of its superconducting coherence length ($\xi_0$). Such nano-superconductors are being investigated for potential applications in nano-electronics and quantum computing. The design of three-dimensional nano-superconductors allows one to conceive novel schemes for such applications. Here, we report for the first time the use of a $He^+$ focused-ion-beam-microscope in combination with the $W(CO)_6$ precursor to grow three-dimensional superconducting hollow nanowires as small as 32 nm in diameter and with an aspect ratio (diameter/length) of as much as 200. Such extreme resolution is achieved by using a small $He^+$ beam spot of 1 nm for the growth of the nanowires. As shown by transmission electron microscopy, they display grains of large size fitting with face-centered cubic $WC_{1-x}$ phase. The nanowires, which are grown vertically to the substrate, are felled on the substrate by means of a nano-manipulator for their electrical characterization. They become superconducting at 6.4 K and show large critical magnetic field and critical current density resulting from their quasi-one-dimensional superconducting

character. These results pave the way for future nanoelectronic devices based on three-dimensional nano-superconductors.

KEYWORDS

helium ion microscope, 3D nanoprinting, tungsten carbide, transmission electron microscopy, magnetotransport measurements, quasi-1D superconductors.

TEXT

Superconducting materials are characterized by the transport of electricity without energy losses, rendering them as highly applicable materials for electrical generators [1], energy storage [2], high-frequency filters and switches [3,4], magnetic sensors [5] and powerful magnets (high magnetic fields) [6]. Nowadays, these superconducting magnets are employed for nuclear magnetic resonance [7], in magnetic resonance imaging [8], in fusion reactors [9] and as part of particle accelerators [10].

The bulk superconductors employed in those applications frequently require nanoscale engineering to achieve the required performance [11]. In fact, when the size of superconductors is reduced to the nanoscale, in the range of their superconducting coherence length ($\xi_0$), novel physical properties emerge [12]. Nano-superconductivity is long established as an important research field allowing applications in quantum computing such as highly-integrated networks of Josephson junctions [13], quantum oscillators based on one-dimensional superconducting nanowires [14] and the study of quantum dynamics based on a single vortex in Josephson junctions [15]. Furthermore, new nanoscale approaches are being explored to preserve the dissipation-free

energy state through the vortex confinement [16] and to fabricate quasi-one-dimensional superconducting nanowire arrays [17].

In the semiconductor industry, novel concepts for advanced nanoelectronic devices have recently exploited the third dimension [18,19]. However, mainly due to the severe complexity to fabricate three-dimensional (3D) nano-superconductors, up to now only a few examples have been reported and implemented in superconducting quantum interference devices [20,21]. Their unique capability to achieve extreme in-plane and out-of-plane magnetic-field sensitivity allows them to be used as a local probe for nanomagnets and nano-superconductors. Hence, the exploitation of the third dimension in nano-superconductivity could represent a paradigm shift for the development of next generation electronic nanodevices with applications in advanced sensing and quantum computing.

The fabrication of 3D nano-objects is challenging and advanced lithography techniques such as those based on focused ion beams (FIB) may be employed. These techniques are actually adequate for creating prototypes in order to investigate new concepts in the field of 3D nano-superconductivity. Over the last decades, the FIB based on a liquid metal ion source of gallium ($Ga^+$) has been the most frequently used, mainly due to its smooth implementation in the current technology, meaning that $Ga^+$ FIB has been exploited for direct writing [22–24] and visualization at the nanoscale. Despite this versatility, $Ga^+$ FIB can have several disadvantages, such as the implantation of Ga atoms into the substrate and its amorphization [25]. Moreover, by adding certain precursor materials, $Ga^+$ FIB is used to grow functional materials in 1D [26], 2D [27] and 3D [28–33] through Focused Ion Beam Induced Deposition (FIBID). Particularly, the use of $Ga^+$ FIB in combination with $W(CO)_6$ as a precursor material has provided superconducting W- based nanostructures in 1D [26,34], 2D [35] and 3D [36–38], with superconducting critical temperature ($T_c$)~ 5

K and upper critical magnetic field ($\mu_0 H_{c2}(0)$)~ 9.5 T. The ability to grow such superconducting W- based nanostructures has also assisted several breakthroughs in vortex physics, in 1D and 2D systems. For the former, the vortex confinement in superconducting W- based nanowires when their lateral size (50 nm) is of comparable value to the intervortex distance and the superconducting coherence length [34]; whereas for the latter, the visualization of the vortex liquid [39], the vortex creep [40] and the order-disorder transition in the vortex lattice at low temperatures [41] have been reported. Despite these advances, $Ga^+$ FIBID suffers from some drawbacks for the growth of continuous and homogeneous in-plane nanowires with lateral size below 50 nm and vertical nanowires with diameter below 100 nm. The lateral/diameter resolution is limited mainly by the beam diameter (~5 nm) and the strong lateral scattering of $Ga^+$ ions, giving rise to a broad spatial range of secondary electrons (SE) that contribute to the deposition process and to a large proximity effect.

A straightforward approach to fabricate superconducting nanostructures with lateral size well below 50 nm could be the use of Focused Electron Beam Induced Deposition (FEBID), given the smaller beam spot achievable at low electron beam currents. However, the utilization of this approach for the growth of superconducting nanostructures is limited to only three relevant studies: (1) MoC nanowires of 100 nm in width, $T_c$= 4 K, precursor gases= $Mo(CO)_6$ + $H_2O$ [42]. (2) W- based wires of 130 nm in width, $T_c$= 2 K, $\mu_0 H_{c2}(0)$= 3.7 T, the electron beam current was 5.1 nA, precursor material= $W(CO)_6$ [43]. (3) Pb- based wires of 1 μm in width, $T_c$= 7.2 K, the electron beam current was > 11 nA, precursor material= $(CH_3CH_2)_4Pb$ [44].

The lack of high resolution in the growth of these wires is likely due to the use of a high beam current. Since the electron beam diameter scales with the beam current, the growth by FEBID

under high current (nA range) will produce a broader beam diameter than Ga-FIB (≈5 nm), limiting the lateral resolution. In addition to this setback, the results reported in [43,44] correspond to inhomogeneous superconducting behavior, which therefore limits their potential.

These disadvantages have led the scientific community to search for the next generation of focused particle beam nano-prototyping. New Gas-FIB sources based on light and noble-ion elements like $He^+$ and $Ne^+$ have been particularly successful, such as in the Helium Ion Microscope (HIM) [45], allowing very small probe size ≈ 0.3 nm. The HIM represents a enormous forward step for higher resolution imaging (0.35 nm) [46,47] and for both, additive and subtractive nanolithography, compared to $Ga^+$ FIB and FEB. Regarding nanolithography, $He^+$ FIB has lower proximity effect [48] and higher sensitivity [49], making it appropriate for milling and growth of sub-10 nm structures [48–51].

In the present work, we report the fabrication of individual vertically-aligned 3D tungsten carbide (WC) crystalline hollow nanowires using a $He^+$ microscope. The resulting hollow nanowire geometry produced by the highly-focused $He^+$ beam makes this single-step nanofabrication method unique for the growth of nanostructures. Their inherent large effective sample surface can confer them a high potential for applications in a broad range of fields. The smallest outer nanowire diameter and longest length were found to be 32 nm and 7 μm, respectively. These WC nanowires display superconductivity below 6.4 K ($T_c$), explained by their large crystal size (20 - 32 nm) and the FCC crystallographic structure, as well as strong upper critical field ($\mu_0 H_{c2}$), and large critical current density ($J_c$). The preparation of such materials with unique properties makes this technique highly relevant for the development of the broad field of 3D nano-superconductivity.

The growth of individual vertically-aligned 3D WC hollow nanowires in a single lithography step from a $W(CO)_6$ precursor occurs by focusing the HIM to ~1 nm whereby the precursor flux is delivered into the process chamber and adsorbs to the substrate, whereas the $He^+$ FIB stays at the same point during the deposition time producing two effects, as depicted in the sketch shown in Figure 1(a). First, the deposition of WC material takes place around the beam incidence point, mainly due to the interaction of secondary electrons (produced by incident and scattered ions) with the precursor molecules adsorbed on the surface and the growing pillar (dark green colour) [52]. Secondly, a cavity is formed at the center of the vertical pillar along its length, giving rise to a hollow nanowire like a non-conventional nanotube (light green colour), caused by the milling produced by the $He^+$ FIB spot (~1 nm) at the incidence point (see Figure S1 in the Supplementary information) [53]. Importantly, the diameter of WC hollow nanowires can be controlled by fine tuning the ion beam current. For example, a 1.15 pA ion current for 5.5 min of deposition time produces 32 nm diameter hollow nanowires (~7 μm in length), whereas a 1.34 pA ion current for 7.8 min of deposition time produces 70 nm diameter nanowires (~3 μm in length) (see Figure 1(b) and Figure S2). The shape uniformity of the WC NW was observed using high-magnification SEM image, depicted in Figure 1(c). Further details regarding growth conditions are described in the Supplementary information (methods section).

Transmission Electron Microscopy (TEM) analysis can confirm the production of WC hollow nanowires. TEM cross-sectional sample preparation [25] was carried out using a FEI Helios Nanolab 650 Dual Beam instrument to obtain further material characterisation. Figure 2(a) shows a high resolution TEM (HRTEM) image of a cross-sectional view of a typical WC hollow nanowire of 32 nm in diameter. The grains observed in these nanowires show diameters between 20 and 32 nm, close to the value of the diameter of the outer nanowire. Notice that TEM cross-

sectional sample preparation can introduce an artefact in the hollow nanowires, refilling the cavity with sputtered material during the milling and polishing processes. Hence, one cannot expect to observe in HRTEM images a hole in the conventional sense. The observed non-uniform circular shape of the cavity at the center of the nanowire is explained by the joint contribution of several adverse effects: a drift of the $He^+$ FIB spot during the nanowire growth, a finite angle formed by the electron beam and the nanowire's axis during the TEM imaging, a partial tilting during the TEM sample preparation with respect to the nanowire section, etc. From this, one can conclude that, under optimum experimental conditions, the diameter of the nanowire cavity could be indeed smaller than the value of 6 nm reported here.

To accurately correlate the crystallographic structure and composition of our hollow nanowires, high-resolution Scanning Transmission Electron Microscopy (HRSTEM) images and Energy Dispersive X-ray Spectroscopy (EDS) spectra were sequentially acquired and processed. Figure 2(b) and (c) show a HRSTEM image of an area of the WC hollow nanowire previously depicted in (a) and the Fast Fourier Transform (FFT) of the squared area in (b), respectively. We index the spots indicated in (c), which correspond to the planes (-1-11), (-200), (-11-1), (-3-11), (02-2), and the [011] zone axis of the $WC_{1-x}$ FCC structure, with a lattice parameter of $a$ = 0.4272 nm. More HR(S)TEM images indexed to the $WC_{1-x}$ structure at two different zone axis, [011] and [112] are shown in Figure S3 and S4 (see the Supplementary information). Composition of the squared area of this WC nanowire revealed that the atomic composition is: 72 % W, 20 % C and 8 % O, with C/W= 0.28. Several EDS spectra were collected in other areas of the WC hollow nanowire (see Figure S5) illustrating that the oxygen content remained almost constant, whereas the carbon content varied from 24 to 10 % (see Table S1) confirming the relatively low C/W ratio [0.13-0.36] (see Supplementary information, where TEM sample

preparation, HR(S)TEM imaging and EDS are also described). Some of the data of composition and temperature stability for the $WC_{1-x}$ FCC phase available in literature are inconsistent and contradictory and the use of advanced characterization techniques to refine the crystallographic structure is highly recommended [54]. This suggests that for non-stoichiometric $WC_{1-x}$ compounds such phase diagram can be modified at the nanoscale. Accordingly, the HR(S)TEM - EDS analysis performed in WC NWs grown by $He^+$ FIBID give some light to the real compositional range in which FCC $WC_{1-x}$ phase could be stable.

In order to place the WC nanowire on top of the dielectric layer for making four-point contacts needed for the subsequent magnetotransport measurements, a nano-manipulator was employed (see Supplementary information for details). This step is quite challenging due to the elastic behavior of the nanowires (see movie in the Supplementary information). Once the WC nanowire is positioned on top of the substrate plane (see Figure 3(a)), four Pt FIBID contacts were grown (see Figure 3(b) and Supplementary information for details of deposition parameters). The same protocol was carried out for thick NWs, as shown in Figure S2.

Four-probe magnetotransport measurements were carried out on individual WC hollow nanowires with a Physical Properties Measurements System (see Supplementary information for details). As indicated in Figure 3(b), the electrical current is established between the outermost contacts and voltage is measured at the inner contacts.

Figure 3(c) shows the normalized resistance ($R/R_N$) as a function of temperature for hollow nanowires of 32 and 70 nm in diameter. The length (L) between the inner contacts is 290 and 395 nm and $R_N$ is their resistance at the normal state (10 K), 1487 Ω and 479.7 Ω, respectively. Thus, their resistivity at the normal state is respectively 398 ± 7 μΩcm and 464 ± 17 μΩcm. Given the difference found in resistivity between both hollow nanowires (≈12 %), it would be

interesting in future to undertake a systematic investigation of the dependence of the resistivity with the diameter of the NW. At low temperature, both nanowires show a sharp resistance drop at $T_c \approx$ 6.4 K (defined as the temperature at which the resistance value is $0.5R_N$), entering the superconducting state. A size dependence of $T_c$ has been found only in nanostructures with dimensions near the critical lengths of the superconducting material [55,56]. Given the high crystalline quality of our WC nanowires, we expect the size dependence of $T_c$ for diameters below 10 nm diameter, in the vicinity of the coherence length value.

For thin NWs, the resistance sharply drops to $\sim 0.1R_N$ at $T_c$ and, below this temperature value, it drops gradually two orders of magnitude more, reaching values below the sensitivity of our measurements. This can be explained considering a second superconducting phase (10 % of the nanowire) with lower $T_c$, which is plausibly justified by either the depression of superconductivity in the NW regions below the two inner Pt FIBID contacts (50 nm in width) [57] or by their proximity effect on the superconductivity [58]. Since the projected range of the $Ga^+$ ions accelerated to 30 keV over the WC nanowires based on Monte Carlo simulation is around 10 nm [59], this could induce some surface artifacts of the thin WC nanowire below the Pt FIBID contacts, decreasing $T_c$. The resistance of the phase with lower $T_c$ in our NW is $\sim 0.1R_N$, which corresponds to a nanowire length of ~33 nm [57], in agreement with the length scale of the damage or proximity effect induced by the growth of the Pt FIBID contacts.

For the 32 nm WC nanowire, Figure 3(d) shows the resistance versus temperature under various values of magnetic field perpendicularly applied. As expected, the superconducting transition shifts to lower temperatures with the magnetic field. A similar dependence is obtained for the 70 nm NW (depicted in Figure S5) and both NWs present a finite resistance at the lowest measured temperature (0.5 K) under high magnetic fields, at 8 T and 9 T for 32 nm NW (see

Figure 3(d)) and at 9 T for 70 nm NW (see Figure S6). As discussed above, this behaviour is justified by the lower values of $T_c$ and $\mu_0 H_{c2}$ in the small region around the Pt-FIBID contacts.

Defining $\mu_0 H_{c2}$ as the value at which the resistance is 0.9 $R_N$, $\mu_0 H_{c2}$ versus temperature is plotted in Figure 4(a) for both NWs. Fitting the data to the power equation (1), which is valid in the proximity of $T_c$,

$$\mu_0 H_{c2}(T) \propto (1 - T/T_c)^n \quad (1)$$

we found that $n$= 0.65 and 0.68 for NWs of 32 nm and $n$= 0.81 for the NW of 70 nm. For two-dimensional multilayered systems with similar thickness or lower than their coherence length, the index $n$ is expected to be 1 and 0.5 for perpendicular and parallel magnetic fields to the surface, respectively [60]. In the case of nanowires and hollow nanowires like non-conventional nanotubes with small diameter, a magnetic field perpendicularly applied to their length will imply that a significant part of the NW surface is indeed parallel to the applied magnetic field. In such a case, hollow nanowires will follow equation (1) but with a modified value of $n$ towards the 0.5 value, as recently observed [61]. By applying equation (1) to the obtained data, we also observed that $n$ deviates from the value of 1 towards 0.5. The dependence of $n$ with $R_N/L$ for the three NWs investigated are shown in the inset of Figure 4(a) [61]. This dependence strongly suggests that the 32 nm NWs are approaching the quasi-one-dimensional superconducting behaviour.

Another relevant result is the finding of large $\mu_0 H_{c2}$ values in comparison with the WC nanowires grown by $Ga^+$ FIB. For instance, at $0.6T_c$, $\mu_0 H_{c2}$ is 6.09 T for WC nanowires of 25 nm in diameter grown by $Ga^+$ FIB [62] whereas it is 8.58 T and 6.85 T respectively for the 32 nm and 70 nm NWs grown by $He^+$ FIB. If equation (1) is extrapolated to low temperatures (T= 0 K), we find $\mu_0 H_{c2}$ values of 13.94 T and 12.91 T, for the 32 nm and 70 nm NWs, respectively, which are

47 % and 36 % higher than the corresponding values in WC nanowires grown by $Ga^+$ FIB [35]. Thus, the use of $He^+$ FIB in the growth of superconducting nanocontacts to nanostructures for electrical measurements under applied magnetic field is a straightforward application of this material given the broad range of magnetic fields accessible. On the other hand, the values of $\mu_0 H_{c2}$ extrapolated to 0 K from equation (1) are higher than the Pauli paramagnetic limit, $\mu_0 H = 1.84 \times T_c = 11.6$ T. This suggests that focused experimental studies are needed in order to find the true values of $\mu_0 H_{c2}$ at low temperatures and the origin of superconductivity breaking under high magnetic fields [63–66].

By applying equation (2), which is valid when $\mu_0 H_{c2}$ is determined by the orbital limit, one can estimate the Cooper pair coherence length, $\xi$. At 4 K, the value of $\xi$ is 6.34 nm and 7.18 nm respectively for the 32 nm and 70 nm NWs and the extrapolated value of $\xi$ at 0 K is 4.86 nm and 5.05 nm respectively, which are comparable to the values obtained in WC nanowires grown by $Ga^+$ FIB [27,35].

$$\mu_0 H_{c2}(T) = \Phi_0 / 2\pi\xi^2(T) \quad (2)$$

where $\Phi_0$ is the magnetic quantum flux. Considering WC NWs as type II superconductors in the weak coupling regime and in the dirty limit, the following expression (3) derived from the Gor'kov theory in the dirty limit [67] can be applied to estimate the magnetic field penetration length ($\lambda$) at zero temperature from the value of $T_c$ and the resistivity in the normal state (these quantities in the International System of Units (SI), as discussed by Kess [68]).

$$\lambda(0) = 1.05 \times 10^{-3} \sqrt{\rho_N / T_c} \quad (3)$$

We find, respectively, $\lambda = 830$ nm and $\lambda = 902$ nm for the 32 nm and 70 nm WC NWs. These values are comparable but slightly higher than those found in the WC nanowires grown by Ga FIB [35].

The critical current density, $J_c$ as a function of the perpendicular applied magnetic field for WC NWs is shown in Figure S7 (see Supplementary information). The highest value of $J_c$~ 0.225 MA/cm$^2$ is found for the thinnest NW (32 nm in diameter) at 0.5 K and 0 T, which is three times higher than that one for thicker NWs (70 nm in diameter). On the other hand, for 70 nm NW, the critical current density follows a decay potential dependence $J_c(B) \propto B^{-\alpha}$ [69], with $\alpha$ = 1.3, which is associated with the collective pinning vortex motion. $J_c$ values are calculated from the critical current, $I_c$ (the value at which the measured voltage is ~100 nV) extracted from the voltage versus current curves for WC NWs shown in the Figure S8 (see Supplementary information).

An interesting feature visible in Figure 4(b) is that $J_c$ is nearly constant at moderate values of applied magnetic field for the 32 nm NW. Defining a value of a characteristic magnetic field (B*) at which $J_c$ is $0.9J_c$ at 0 T [70], we find that B*= 2.63 T for the 32 nm NW. In fact, B* is very high and we sketch a plausible scenario of the vortex configuration in the NW illustrated in the inset of Figure 4(b). For B< B* the intervortex distance, $d$> 30 nm, calculated from $d = (4/3)^{1/4}(\Phi_0/B)^{1/2}$, indicating that the critical current density could be determined by the strong confinement potential of a single row of vortices at the center of our hollow nanowire. This effect has been recently reported in ultranarrow nanowires [34,71]. Compared to the nanowires, a stronger confinement potential is expected for hollow nanowires given that the hole at the center is a low-energy location for the vortex. On the other hand, for B> B*, the critical current density follows a decay potential dependence $J_c(B) \propto B^{-\alpha}$ [69] as already shown for 70 nm NW, with $\alpha = 2$, which is associated with the collective pinning vortex motion. Thus, for B> B*, the vortex interaction is very strong given the small intervortex distance (< 30 nm), it competes with the

confinement potential and produces the faster decay of the critical current with the magnetic field.

In conclusion, we report a novel methodology for the fabrication of individual 3D superconducting crystalline WC hollow nanowires by decomposing a $W(CO)_6$ precursor using a highly-focused $He^+$ microscope, that could serve as building blocks for future 3D superconducting nanodevices. The resulting crystalline nanowires conform to the FCC $WC_{1-x}$ phase ($0.13<x<0.36$) and possess outer diameters as small as 32 nm with aspect ratios of *ca.* 200, which is in general impossible to achieve with other nanofabrication techniques. By studying their magnetotransport properties, we have found that they exhibit superconducting properties below $T_c$= 6.4 K, as well as high critical magnetic field ($\mu_0 H_{c2}$) and critical current density ($J_c$). The $T_c$ and $\mu_0 H_{c2}$ values are 1.5 times higher than those reported for WC nanowires of similar dimensions grown by $Ga^+$ FIB and the temperature dependence of $\mu_0 H_{c2}$ and the field dependence of $J_c$ indicate that the smallest hollow nanowires behave as quasi-one-dimensional superconductors. Further, the robust superconductivity shown by these nanowires in a broad range of applied magnetic field and current and the lower proximity effect of the $He^+$ FIB will allow detailed studies in nano-superconductivity as well as their application for creating superconducting nanocontacts to nanostructures, for building vortex-based nanodevices and highly-dense superconducting nanowire arrays. In addition, given that the technique directs the growth of complex 3D structures [72], one can anticipate the creation of various other more sophisticated 3D superconducting nanostructures of specific relevance to the field of 3D nano-superconductivity.

FIGURES

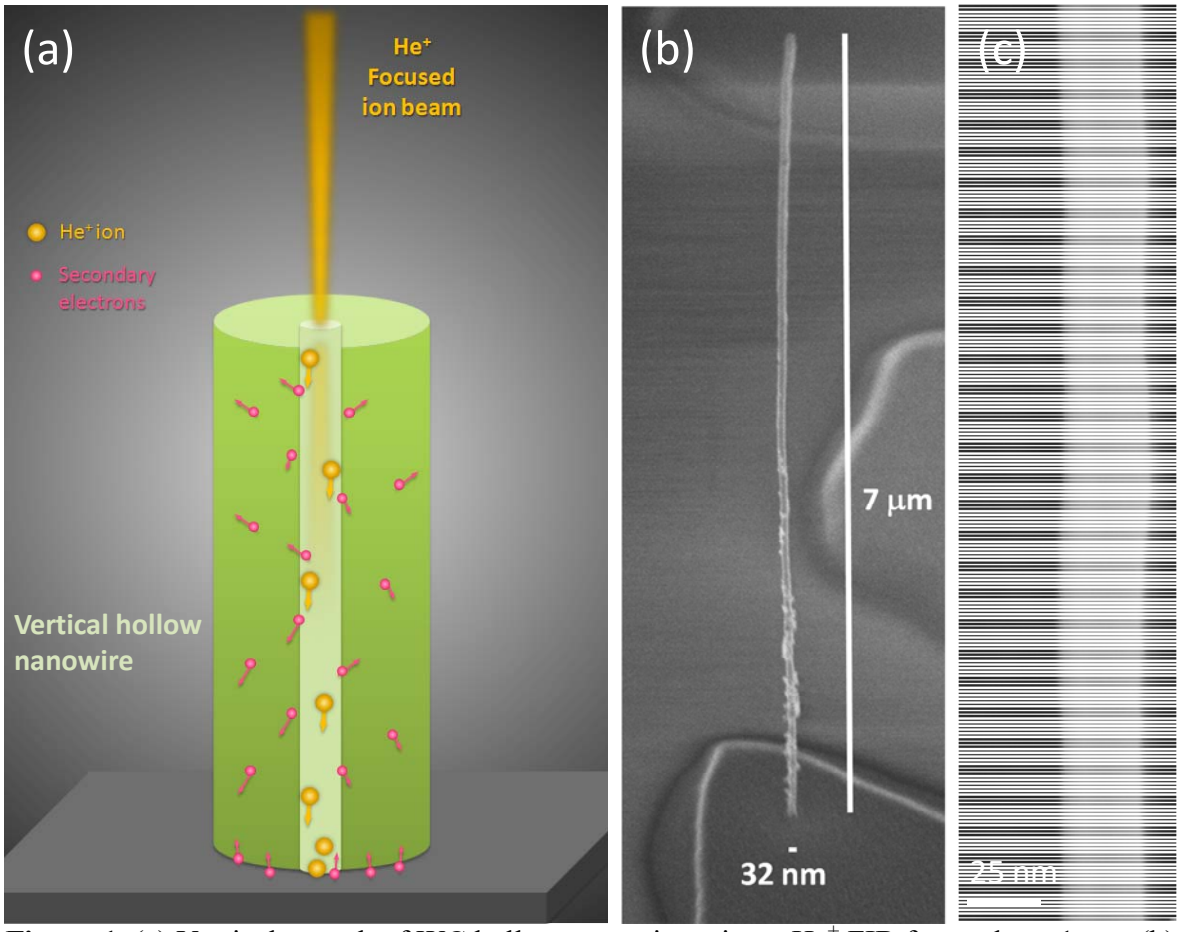


**Figure 1.** (a) Vertical growth of WC hollow nanowire using a $He^+$ FIB focused to ~1 nm. (b) SEM image of a vertical 3D WC hollow nanowire (52º tilted stage). (c) High magnification SEM image of the WC nanowire.

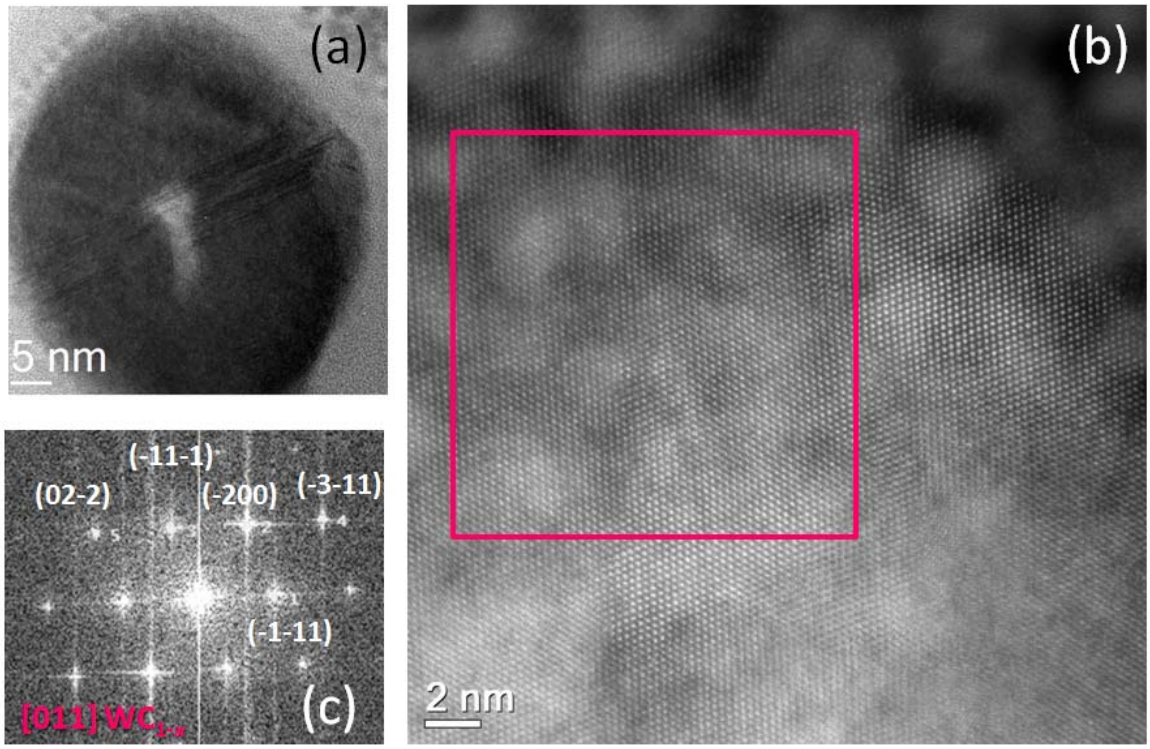


**Figure 2.** (a) HRTEM image of a cross sectional view of a typical WC hollow nanowire. (b) HR(S)TEM image of a cross-sectional view of the WC nanowire in (a). (c) The Fast Fourier Transform of the squared area in (b), showing the crystalline nature of the material and indexed as the [011] zone axis of the FCC $WC_{1-x}$ structure.

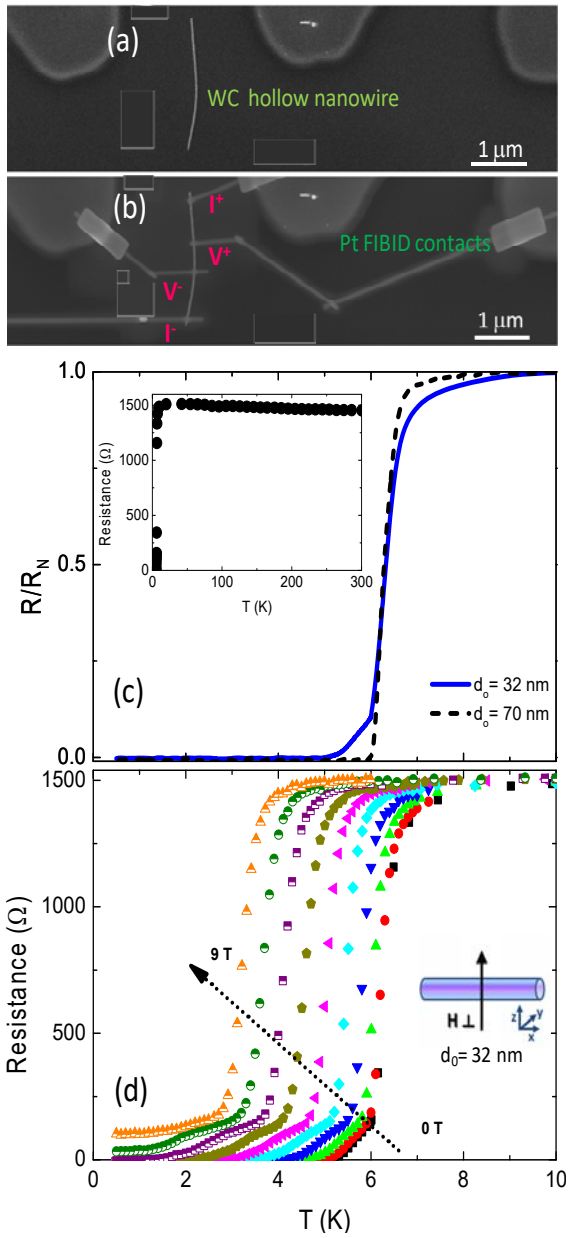


**Figure 3.** (a) SEM image of a WC hollow nanowire situated on the substrate plane. (b) SEM image of a WC nanowire connected to the pre-patterned Ti pads by using four Pt FIBID contacts. (c) Normalized resistance for WC NWs of 32 and 70 nm in diameter as function of temperature at 0 T. Inset shows resistance versus temperature for thin WC nanowire ($d_o$= 32 nm). (d) Resistance as a function of temperature for thin WC nanowire ($d_o$= 32 nm) under perpendicular magnetic field, from 0 to 9 T.

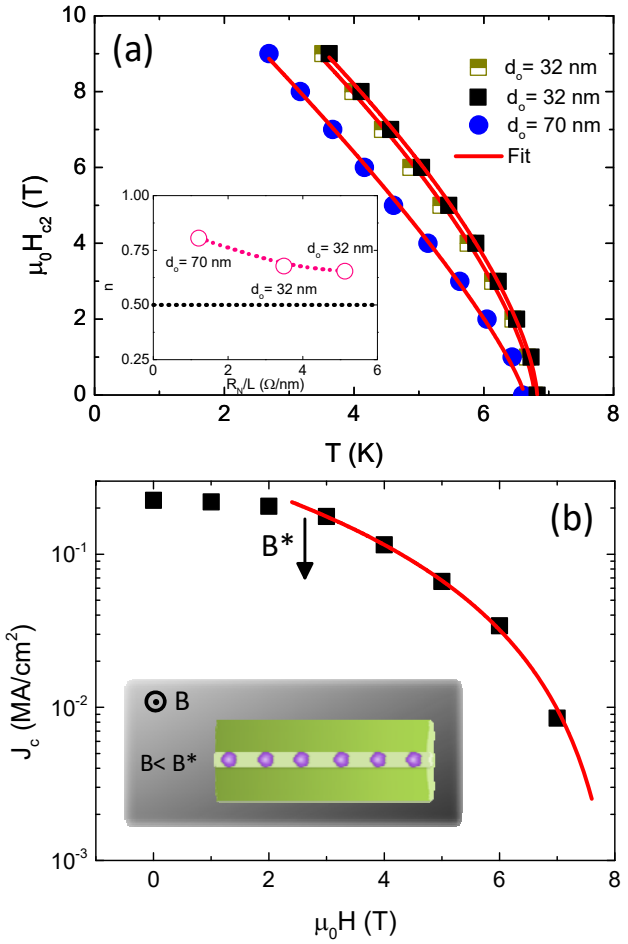


**Figure 4.** (a) Upper critical magnetic field ($\mu_0 H_{c2}$) as a function of temperature for WC hollow nanowires (two of them with outer diameter of 32 and one of 70 nm). Data is fitted to a potential equation (1). Inset shows the dependence of the index *n* (from the equation (1)) with $R_N/L$. (b) Critical current density ($J_c$) as a function of the applied magnetic field at 0.5 K for a WC hollow nanowire of 32 nm in outer diameter. Data above B* (field value at which $J_c$ is $0.9J_c$ at 0 T) is fitted to a potential equation characteristic of collective vortex pinning (see main text). Inset illustration shows how the magnetic flux penetrates into the hollow nanowire, as a single vortex row at B<B*. The purple circles indicate the vortex row.

ASSOCIATED CONTENT

**Supporting Information**.

Methods: growth of WC hollow nanowires, nano-manipulation of WC hollow nanowires, growth of auxiliary Pt FIBID nanocontacts, magnetotransport measurements, microstructure and composition at the nanoscale.

Movie - video of elastic behaviour of WC hollow nanowires.

SEM images of WC nanowire with 70 nm in outer diameter.

Microstructure and composition of WC hollow nanowires.

Magnetotransport measurements on WC hollow nanowire of 70 nm in outer diameter (R vs T, V vs I, dV/dI vs I under perpendicular magnetic field).

Curves of $J_c$ vs B, for WC NWs of 32 and 70 nm in outer diameter.

Curves of V vs I, dV/dI vs I under perpendicular magnetic field for WC NW of 32 nm in outer diameter.

The following files are available free of charge.

AUTHOR INFORMATION

**Corresponding Author**

* Address correspondence to Rosa Córdoba (rosa.cordoba.castillo@gmail.com) and José Mª De Teresa (deteresa@unizar.es).

**Author Contributions**

R. C. and J. M. D. T conceived the experiments. R. C. and D. M. grew the WC hollow nanowires by using a $He^+$ microscope. A. I. acquired and performed the analysis of the HR(S)TEM images and EDS spectra. R.C. made the auxiliary contacts to the WC NWs, measured their electrical transport behavior, performed the subsequent data analysis and wrote the first version of the manuscript. All authors discussed the results, the manuscript, contributed to it and have given approval to the final version of the manuscript.

**Funding Sources**

This work was supported by the financial support from Spanish Ministry of Economy and Competitiveness through the projects MAT2014-51982-C2-1-R, MAT2014-51982-C2-2-R, MAT2017-82970-C2-2-R, and from regional Gobierno de Aragón through project E26 and E81 with European Social Fund. R.C. acknowledges Juan de la Cierva-Incorporación 2014 program. This project has received funding from the EU-H2020 research and innovation programme under grant agreement No 654360 NFFA-Europe.

ACKNOWLEDGMENT

This work was supported by the financial support from Spanish Ministry of Economy and Competitiveness through the projects MAT2014-51982-C2-1-R, MAT2014-51982-C2-2-R, MAT2017-82970-C2-2-R, and from regional Gobierno de Aragón through project E26 and E81 with European Social Fund. R.C. acknowledges Juan de la Cierva-Incorporación 2014 program. Authors strongly acknowledge Laura Casado and Isabel Rivas for TEM sample preparation and for the nano-manipulation of the WC nanotubes; Rubén Valero for the UV lithography process;

and Scott Mitchell for reading and addressing some language issues in the manuscript. The microscopy works have been conducted in the "Laboratorio de Microscopías Avanzadas" at "Instituto de Nanociencia de Aragon - Universidad de Zaragoza". Authors acknowledge the LMA-INA for offering access to their instruments and expertise. Authors would like to acknowledge the use of Servicio General de Apoyo a la Investigación-SAI, Universidad de Zaragoza, particularly the Servicio de Medidas Físicas. This project has received funding from the EU-H2020 research and innovation programme under grant agreement No 654360 NFFA-Europe.

REFERENCES

(1) Barnes, P. N.; Sumption, M. D.; Rhoads, G. L. *Cryogenics (Guildf).* **2005**, *45* (10–11), 670–686.

(2) Larbalestier, D.; Gurevich, A.; Feldmann, D. M.; Polyanskii, A. *Nature* **2001**, *414* (6861), 368–377.

(3) Martinez, J.; Hijazi, Y.; Brzhezinskaya, M.; Bogozi, A.; Noel, J.; Vlasov, Y. A.; Larkins, G. L. *Phys. C Supercond.* **2007**, *466* (1–2), 101–105.

(4) Noel, J.; Hijazi, Y.; Martinez, J.; Vlasov, Y. A.; LarkinsJr, G. L. *Supercond. Sci. Technol.* **2003**, *16* (12), 1438–1441.

(5) Tesche, C. D.; Clarke, J. *J. Low Temp. Phys.* **1977**, *29* (3–4), 301–331.

(6) Larbalestier, D. C.; Jiang, J.; Trociewitz, U. P.; Kametani, F.; Scheuerlein, C.; Dalban-Canassy, M.; Matras, M.; Chen, P.; Craig, N. C.; Lee, P. J.; Hellstrom, E. E. *Nat. Mater.* **2014**, *13* (4), 375–381.

(7) Reif, F. *Phys. Rev.* **1956**, *102* (5), 1417–1418.

(8) Eccles, C. .; Callaghan, P. . *J. Magn. Reson.* **1986**, *68* (2), 393–398.

(9) Bromberg, L.; Tekula, M.; El-Guebaly, L. .; Miller, R. *Fusion Eng. Des.* **2001**, *54* (2), 167–180.

(10) Schmuser, P. *Reports Prog. Phys.* **1991**, *54* (5), 683–730.

(11) Gutiérrez, J.; Llordés, A.; Gázquez, J.; Gibert, M.; Romà, N.; Ricart, S.; Pomar, A.; Sandiumenge, F.; Mestres, N.; Puig, T.; Obradors, X. *Nat. Mater.* **2007**, *6* (5), 367–373.

(12) Arutyunov, K. Y.; Golubev, D. S.; Zaikin, A. D. *Phys. Reports-Review Sect. Phys. Lett.* **2008**, *464* (1–2), 1–70.

(13) Fazio, R. *Phys. Rep.* **2001**, *355* (4), 235–334.

(14) Giordano, N. *Phys. Rev. Lett.* **1988**, *61* (18), 2137–2140.

(15) Wallraff, A.; Lukashenko, A.; Lisenfeld, J.; Kemp, A.; Fistul, M. V.; Koval, Y.; Ustinov, A. V. *Nature* **2003**, *425* (6954), 155–158.

(16) Tonomura, A.; Kasai, H.; Kamimura, O.; Matsuda, T.; Harada, K.; Nakayama, Y.; Shimoyama, J.; Kishio, K.; Hanaguri, T.; Kitazawa, K.; Sasase, M.; Okayasu, S. *Nature* **2001**, *412* (6847), 620–622.

(17) Xu, K.; Heath, J. R. *Nano Lett.* **2008**, *8* (1), 136–141.

(18) Goldberger, J.; Hochbaum, A. I.; Fan, R.; Yang, P. *Nano Lett.* **2006**, *6* (5), 973–977.

(19) Shulaker, M. M.; Hills, G.; Park, R. S.; Howe, R. T.; Saraswat, K.; Wong, H.-S. P.; Mitra, S. *Nature* **2017**, *547* (7661), 74–78.

(20) Finkler, A.; Vasyukov, D.; Segev, Y.; Neeman, L.; Anahory, Y.; Myasoedov, Y.; Rappaport, M. L.; Huber, M. E.; Martin, J.; Yacoby, A.; Zeldov, E. *J. Phys. Conf. Ser.* **2012**, *400* (5), 52004.

(21) Anahory, Y.; Reiner, J.; Embon, L.; Halbertal, D.; Yakovenko, A.; Myasoedov, Y.; Rappaport, M. L.; Huber, M. E.; Zeldov, E. *Nano Lett.* **2014**, *14* (11), 6481–6487.

(22) Kato, T. *J. Vac. Sci. Technol. B Microelectron. Nanom. Struct.* **1985**, *3* (1), 50.

(23) Blauner, P. G.; Ro, J. S.; Butt, Y.; Melngailis, J. *J. Vac. Sci. Technol. B* **1989**, *7* (4), 609–617.

(24) Gierak, J.; Madouri, A.; Biance, A. L.; Bourhis, E.; Patriarche, G.; Ulysse, C.; Lucot, D.; Lafosse, X.; Auvray, L.; Bruchhaus, L.; Jede, R. *Microelectron. Eng.* **2007**, *84* (5–8), 779–783.

(25) Giannuzzi, L. A.; Stevie, F. A. *Introduction to focused ion beams*; Science, S., Ed.; Springer Science: Boston, 2005.

(26) Li, W.; Fenton, J. C.; Gu, C.; Warburton, P. A. *Microelectron. Eng.* **2011**, *88* (8), 2636–2638.

(27) Guillamón, I.; Suderow, H.; Vieira, S.; Fernández-Pacheco, A.; Sesé, J.; Córdoba, R.; De Teresa, J. M.; Ibarra, M. R. *New J. Phys.* **2008**, *10* (9), 93005.

(28) Matsui, S.; Kaito, T.; Fujita, J.; Komuro, M.; Kanda, K.; Haruyama, Y. In *Papers from the 44th international conference on electron, ion, and photon beam technology and nanofabrication*; AVS: Rancho Mirage, California, (USA), 2000; Vol. 18, pp 3181–3184.

(29) Morita, T.; Kometani, R.; Watanabe, K.; Kanda, K.; Haruyama, Y.; Hoshino, T.; Kondo, K.; Kaito, T.; Ichihashi, T.; Fujita, J.; Ishida, M.; Ochiai, Y.; Tajima, T.; Matsui, S. *J. Vac. Sci. Technol. B Microelectron. Nanom. Struct.* **2003**, *21* (6), 2737.

(30) Esposito, M.; Tasco, V.; Todisco, F.; Benedetti, A.; Sanvitto, D.; Passaseo, A. *Adv. Opt. Mater.* **2014**, *2* (2), 154–161.

(31) Esposito, M.; Tasco, V.; Cuscun, M.; Todisco, F.; Benedetti, A.; Tarantini, I.; Giorgi, M. De; Sanvitto, D.; Passaseo, A. *ACS Photonics* **2015**, *2* (1), 105–114.

(32) Fujii, T.; Iwasaki, K.; Munekane, M.; Takeuchi, T.; Hasuda, M.; Asahata, T.; Kiyohara, M.; Kogure, T.; Kijima, Y.; Kaito, T. *J. Micromechanics Microengineering* **2005**, *15* (10), S286–S291.

(33) Nakai, Y.; Kang, Y.; Okada, M.; Haruyama, Y.; Kanda, K.; Ichihashi, T.; Matsui, S. *Jpn. J. Appl. Phys.* **2010**, *49* (6), 06GH07.

(34) Córdoba, R.; Baturina, T. I.; Sesé, J.; Mironov, A. Y.; De Teresa, J. M.; Ibarra, M. R.; Nasimov, D. A.; Gutakovskii, A. K.; Latyshev, A. V.; Guillamón, I.; Suderow, H.; Vieira, S.; Baklanov, M. R.; Palacios, J. J.; Vinokur, V. M. *Nat. Commun.* **2013**, *4* (1), 1437.

(35) Sadki, E. S.; Ooi, S.; Hirata, K. *Appl. Phys. Lett.* **2004**, *85* (25), 6206–6208.

(36) Li, W.; Gu, C.; Warburton, P. A. *J. Nanosci. Nanotechnol.* **2010**, *10* (11), 7436–7438.

(37) Romans, E. J.; Osley, E. J.; Young, L.; Warburton, P. A.; Li, W. *Appl. Phys. Lett.* **2010**, *97* (22), 222506.

(38) Li, W.; Fenton, J. C.; Cui, A.; Wang, H.; Wang, Y.; Gu, C.; McComb, D. W.; Warburton, P. A. *Nanotechnology* **2012**, *23* (10), 105301.

(39) Guillamón, I.; Suderow, H.; Fernández-Pacheco, A.; Sesé, J.; Córdoba, R.; De Teresa, J. M.; Ibarra, M. R.; Vieira, S. *Nat. Phys.* **2009**, *5* (9), 651–655.

(40) Guillamón, I.; Suderow, H.; Vieira, S.; Sesé, J.; Córdoba, R.; De Teresa, J. M.; Ibarra, M. R. *Phys. Rev. Lett.* **2011**, *106* (7), 77001.

(41) Guillamón, I.; Córdoba, R.; Sesé, J.; De Teresa, J. M.; Ibarra, M. R.; Vieira, S.; Suderow, H. *Nat. Phys.* **2014**, *10* (11), 851–856.

(42) Makise, K.; Mitsuishi, K.; Shimojo, M.; Shinozaki, B. *Sci. Rep.* **2015**, *4* (1), 5740.

(43) Sengupta, S.; Li, C.; Baumier, C.; Kasumov, A.; Guéron, S.; Bouchiat, H.; Fortuna, F. *Appl. Phys. Lett.* **2015**, *106* (4), 42601.

(44) Winhold, M.; Weirich, P. M.; Schwalb, C. H.; Huth, M. *Appl. Phys. Lett.* **2014**, *105* (16), 162603.

(45) Scipioni, L.; Stern, L. A.; Notte, J.; Sijbrandij, S.; Griffin, B. *Adv. Mater. Process.* **2008**, *166* (6), 27.

(46) Bell, D. C. *Microsc. Microanal.* **2009**, *15* (2), 147–153.

(47) Alkemade, P. F. A.; Koster, E. M.; van Veldhoven, E.; Maas, D. J. *Scanning* **2012**, *34* (2), 90–100.

(48) Maas, D.; van Veldhoven, E.; Chen, P.; Sidorkin, V.; Salemink, H.; van der Drift, E.; Alkemade, P. In *Metrology, Inspection, and Process Control for Microlithography Xxiv*; Raymond, C. J., Ed.; 2010; Vol. 7638.

(49) Sidorkin, V.; van Veldhoven, E.; van der Drift, E.; Alkemade, P.; Salemink, H.; Maas, D. *J. Vac. Sci. Technol. B Microelectron. Nanom. Struct.* **2009**, *27* (4), L18.

(50) Baglin, J. E. E. *Appl. Surf. Sci.* **2012**, *258* (9), 4103–4111.

(51) Wu, H.; Stern, L. A.; Xia, D.; Ferranti, D.; Thompson, B.; Klein, K. L.; Gonzalez, C. M.; Rack, P. D. *J. Mater. Sci. Mater. Electron.* **2014**, *25* (2), 587–595.

(52) Chen, P.; van Veldhoven, E.; Sanford, C. a; Salemink, H. W. M.; Maas, D. J.; Smith, D. a; Rack, P. D.; Alkemade, P. F. A. *Nanotechnology* **2010**, *21* (45), 455302.

(53) Kohama, K.; Iijima, T.; Hayashida, M.; Ogawa, S. *J. Vac. Sci. Technol. B Microelectron. Nanom. Struct.* **2013**, *31* (3), 31802.

(54) Kurlov, A. S.; Gusev, A. I. *Inorg. Mater.* **2006**, *42* (2), 121–127.

(55) Smith, R. A.; Handy, B. S.; Ambegaokar, V. *Phys. Rev. B* **2001**, *63* (9), 94513.

(56) Guo, Y.; Zhang, Y.-F.; Bao, X.-Y.; Han, T.-Z.; Tang, Z.; Zhang, L.-X.; Zhu, W.-G.; Wang, E. G.; Niu, Q.; Qiu, Z. Q.; Jia, J.-F.; Zhao, Z.-X.; Xue, Q.-K. *Science (80-. ).* **2004**, *306* (5703).

(57) Tian, M.; Wang, J.; Ning, W.; Mallouk, T. E.; Chan, M. H. W. *Nano Lett.* **2015**, *15* (3), 1487–1492.

(58) Kasumov, A.; Kociak, M.; Ferrier, M.; Deblock, R.; Guéron, S.; Reulet, B.; Khodos, I.; Stéphan, O.; Bouchiat, H. *Phys. Rev. B* **2003**, *68* (21), 214521.

(59) Ziegler, J. F.; Biersack, J. P.; Littmark, U. *The Stopping and Range of Ions in Solids*; Pergamon Press: New York, 1985.

(60) Tinkham, M. *Introduction to Superconductivity*, Second.; Dover Publications, Inc., 1996.

(61) Makise, K.; Terai, H.; Tominari, Y.; Tanaka, S.; Shinozaki, B. *Sci. Rep.* **2016**, *6* (1),

27001.

(62) Córdoba, R.; Ibarra, A; De Teresa, J. M. *manuscript in preparation*.

(63) Orlando, T. P.; McNiff, E. J.; Foner, S.; Beasley, M. R. *Phys. Rev. B* **1979**, *19* (9), 4545–4561.

(64) Gor 'kov, L. P. *J. Exptl. Theor. Phys.* **1960**, *37* (37), 1407–1416.

(65) Larkin, A. I.; Ovchinnikov, Y. N. *Zhurnal Eksp. I Teor. Fiz.* **1975**, *68* (5), 1915–1927.

(66) Fulde, P.; Ferrell, R. A. *Phys. Rev.* **1964**, *135* (3A), A550.

(67) Gor 'kov, L. P. *J. Exptl. Theor. Phys.* **1959**, *36* (36), 1918–1923.

(68) Kes, P. H.; Tsuei, C. C. *Phys. Rev. B* **1983**, *28* (9), 5126–5139.

(69) Dam, B.; Huijbregtse, J. M.; Klaassen, F. C.; van der Geest, R. C. F.; Doornbos, G.; Rector, J. H.; Testa, A. M.; Freisem, S.; Martinez, J. C.; Stäuble-Pümpin, B.; Griessen, R. *Nature* **1999**, *399* (6735), 439–442.

(70) Ozaki, T.; Wu, L.; Zhang, C.; Jaroszynski, J.; Si, W.; Zhou, J.; Zhu, Y.; Li, Q. *Nat. Commun.* **2016**, *7*, 13036.

(71) Morgan-Wall, T.; Leith, B.; Hartman, N.; Rahman, A.; Marković, N. *Phys. Rev. Lett.* **2015**, *114* (7), 77002.

(72) Fowlkes, J. D.; Winkler, R.; Lewis, B. B.; Stanford, M. G.; Plank, H.; Rack, P. D. *ACS Nano* **2016**, *10* (6), 6163–6172.